Available online at www.sciencedirect.com
SCIENCE DIRECT®
C. R. Chimie 6 (2003) 919–934
COMPTES RENDUS CHIMIE

Dendritic nanodevices

Electrochemical deposition of metal nanoparticles functionalized with multiple redox molecules

Mami Yamada †, Hiroshi Nishihara *

Department of Chemistry, School of Science, The University of Tokyo, 7-2-3, Hongo, Bunkyo-ku, Tokyo 113-0033, Japan

Received 3 March 2003; accepted 22 July 2003

Abstract

The electrodeposition of metal nanoparticles, the surface of which was functionalized with multiple redox species, biferrocene (BFc) or anthraquinone (AQ) thiol derivatives, proceeded to construct a redox-active metal nanoparticle film on an electrode. The investigation of this deposition mechanism was carried out with electrochemical (CV, EQCM) and spectroscopic (UV–Vis) measurements, elemental analysis (ICP, PGA), and surface observations of the formed films (STM, AFM). It was demonstrated that this system could be utilized as a novel method for fabricating versatile metal nanoparticle films comprised of multiple layers by changing parameters in the deposition process such as the solvent, core element, and core size. The specific spectroscopic properties of the prepared films induced by particle-particle interactions different from those induced by isolated particles are also discussed herein. ***To cite this article: M. Yamada, H. Nishihara, C. R. Chimie 6 (2003).***

© 2003 Published by Éditions scientifiques et médicales Elsevier SAS on behalf of Académie des sciences.

Keywords: nanoparticle; redox; ferrocene; anthraquinone; surface plasmon; deposition; assembly

1. Introduction

Much research is now in progress attempting to identify more useful materials for electronic devices in microelectronics. In this field, a high level of interest has arisen with regard to nanometer-sized metal and semiconductor particles (nanoparticles) [1–6], which are expected to have diverse applications in optoelectronic devices [7, 8] and as molecular catalysts [9, 10] and chemical sensors [11] based primarily on their quantum size effect (QSE) [12]. To gather more information about these advanced materials, we attempted to combine the prominent properties of metal nanoparticles and functional molecules onto the particle surface, expecting that the character of the metal core could be controlled by the electronic state of surrounding functional species, which were reversibly converted with the simulation of an electronic field [13, 14] and light [15, 16]. Here the redox-active species were selected as functional molecules, especially multiple-redox units. These compounds allowed an enormous charge accumulation on the metal nanoparticle, which could significantly irritate the electronic

* Corresponding author.
E-mail addresses: myamada@jaist.ac.jp (M. Yamada), nisihara@chem.s.u-tokyo.ac.jp (H. Nishihara).
† Present address: Department of Physical Materials Science, School of Materials Science, Japan Advanced Institute of Science and Technology (JAIST), 1-1, Asahidai, Tatsunokuchi-machi, Nomi-gun, Ishikawa 923-1211, Japan.

© 2003 Published by Éditions scientifiques et médicales Elsevier SAS on behalf of Académie des sciences.
doi:10.1016/j.crci.2003.07.005

condition of the metal core. The two contrastive molecules, the biferrocene (BFc) and anthraquinone (AQ) derivatives, were introduced onto a metal nanoparticle (Scheme 1); in particular, the former undergoes a two-step one-electron 'oxidative' reaction of $BFc/BFc^{+}/BFc^{2+}$ in electrolyte solution, while the latter undergoes a two-step one-electron 'reductive' reaction of $AQ/AQ^{-}/AQ^{2-}$.

The BFc or AQ-modified gold nanoparticles (Au_n-BFc [17–19] and Au_n-AQ [20, 21], respectively) were prepared by a thiolate exchange reaction [22–24] between an alkyl thiolate-stabilized metal nanoparticle (Au_n-AT) and a functional thiol derivative (1-(9-thiononyl-1-one)-1',1''-biferrocene: BFcS and 1-(1,8-dithiaoctyl)anthracene-9,10-dione: AQS, respectively) in organic solvent (e.g. CH_2Cl_2, toluene, THF). The second oxidation process of BFc units of Au_n-BFc in electrolyte solution led to the formation of a uniform redox-active gold nanoparticle film on an electrode; in contrast, Au_n-AQ was found to be aggregated by two-electron reduction of AQ sites, clarifying that metal nanoparticles functionalized with multiple-redox molecules can assemble according to the charge accumulation of redox species on a particle/solution interface. Note that the multiple-electron system seems indispensable for these deposition phenomena, as they are not observed for particles with a single redox species such as ferrocene [22]. These results suggest that a detailed elucidation of the assembly mechanism should be a primary focus of current scientific interest. In addition, this system exhibits a promising possibility for constructing versatile redox-active nanoparticle films on an electrode by the changing of several deposition parameters.

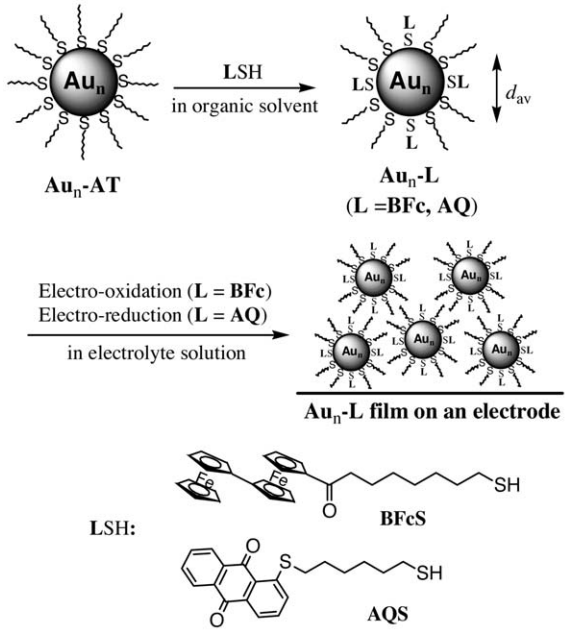

Scheme 1. Preparation and electrodeposition of Au_n-BFc and Au_n-AQ.

In this account, the overviewed electrodeposition phenomena of Au_n-BFc and Au_n-AQ are presented with morphological, optical, and spectroelectrochemical aspects of the deposited redox species-immobilized gold nanoparticles. In particular, the mechanistic analysis of electro-oxidative deposition phenomenon of Au_n-BFc are described along with the deposition dependence for film formation on core size, electrolyte, solvent, and core metal element (the BFc-attached palladium nanoparticle; Pd_n-BFc [25]), leading to the fabrication of alternating gold and palladium nanoparticle film as a practical application.

2. Film formation of metal nanoparticles modified with multiple redox species

2.1. Electro-oxidative deposition process of M_n-BFc (M = Au, Pd)

2.1.1. Au_n-BFc: dependence on core size, electrolyte, and solvent

Au_n-ATs were prepared in two ways: one was the Brust method [26], using reduction of $HAuCl_4$ with a tenfold excess of $NaBH_4$ in the presence of octanethiol in a water/toluene mixture for the compounds of **1, 2, 3**, and **4** in Table 1. The average core diameter, d_{av}, of Au_n-AT thus prepared was determined by transmission electron microscopy (TEM, Fig. 1), altered by changing the molar ratio of $HAuCl_4$ to octanethiol under synthetic conditions [27]. The other method for the synthesis of **5** was based on Sorensen's report [28], carried out in single toluene phase where the ammonium salt-stabilized gold nanoparticles were synthesized, followed by an exchange reaction with dodecanethiol. The UV–Vis spectra of **2, 3, 4**, and **5** in CH_2Cl_2 exhibit a surface plasmon (SP) band at ca. 520 nm ($\varepsilon_{max} = 7.7 \times 10^5$ $M^{-1}cm^{-1}$, $\varepsilon_{max} = 2.4 \times 10^6$ $M^{-1}cm^{-1}$, $\varepsilon_{max} = 2.8 \times 10^6$ $M^{-1}cm^{-1}$, and $\varepsilon_{max} = 7.8 \times 10^6$ $M^{-1}cm^{-1}$ [27], respectively), while that of **1** shows

Table 1
Size and composition results for different methods of Au_n-BFc preparation

Compound	Feed ratio of thiol to $HAuCl_4$	Core diameter[a] d_{av} (nm)	Standard deviation[a] d_{sd} (nm)	Number of Au atoms[b]	Number of thiol on the Au surface[b]	Number ratio of thiolate to BFcS[c]	θ_{Bfc}[c]
1	1:0.5	1.7	0.5	201	71	14.0	4.7
2	1:1	2.3	0.5	309	92	11.3	3.6 7.5 15.0
3	1:4	2.9	0.8	976	187	8.0	20.8
4	1:12	4.3	1.1	2951	371	32	11.3
5	—	6.4	0.8	8100	600	107	4.6

[a] Determined by TEM images.
[b] See [21]. Regarding **5**, the approximate number of Au atoms, N_{Au}, can be calculated in the equation of N_{Au}= (59 nm^{-3}) (π/6) (d_{av}/2)^3 where 59 nm^{-3} is the density (59 atoms/nm^3) of bulk fcc-Au. The number of dodecyl thiolate on a metal core surface was estimated as 600, assuming that the occupied area of one thiolate on a particle is 21.4 $Å^2$, the value for which is based on a bulk Au (111) surface.
[c] Determined by ^{1}H-NMR spectra.

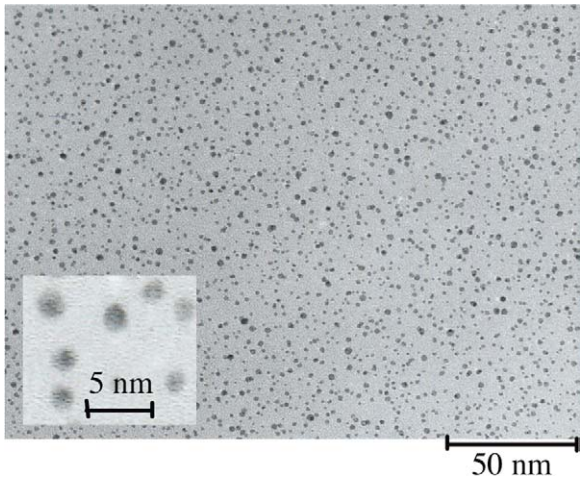

Fig. 1. TEM image of **2** (θ_{BFc} = 7.5).

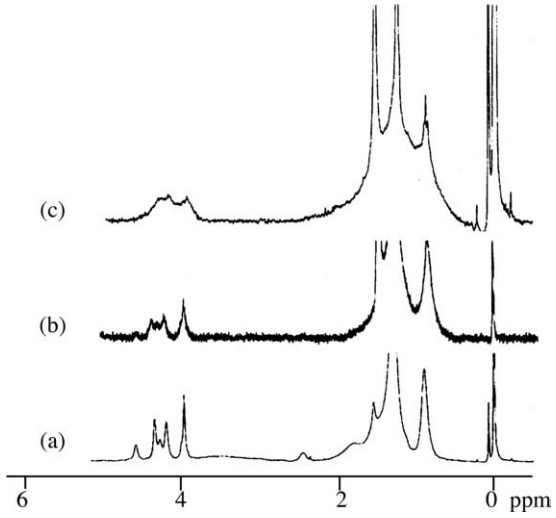

Fig. 2. ^{1}H-NMR spectra of (a) **1**, (b) **2** (θ_{BFc} = 7.5), and (c) **3** in $CDCl_3$.

only a gentle curve attributed to the Mie scattering [25] due to the QSE [29]. The number of exchanged BFcS on the Au_n-AT surface, θ_{BFc}, was calculated based on the ratio of the integrals of the ^{1}H-NMR signals between BFc and methyl protons at 3.9–4.7 ppm and 0.8–0.9 ppm, respectively (Fig. 2). As for **2**, the exchange rate was controlled by the molar ratio of BFcS to Au_n-AT in the exchange reaction.

Fig. 3A shows the typical cyclic voltammograms of **3** in the electrodeposition process, which is measured in a solution of **3** at an indium tin oxide (ITO) electrode in Bu_4NClO_4–CH_2Cl_2. The peak current increases gradually by consecutive potential scans between –0.3 and 0.9 V vs. Ag/Ag^+, where two-step one-electron oxidation due to BFc units on a particle surface occurs at 0.20 and 0.61 V vs. Ag/Ag^+, suggesting that Au_n-BFc particles accumulate on an electrode/solution interface by two-electron oxidation of BFc sites. UV–Vis spectra of Au_n-BFc films thus prepared exhibit broad absorption bands that grow in intensity with increases in the number of potential scans (Fig. 3B); the film thickness can also be controlled by changing the number of potential scans. Cyclic voltammograms of the electrode films in a pure electrolyte solution show two pairs of cathodic and anodic waves (Fig. 3B, inset), the peak currents of which are propor-

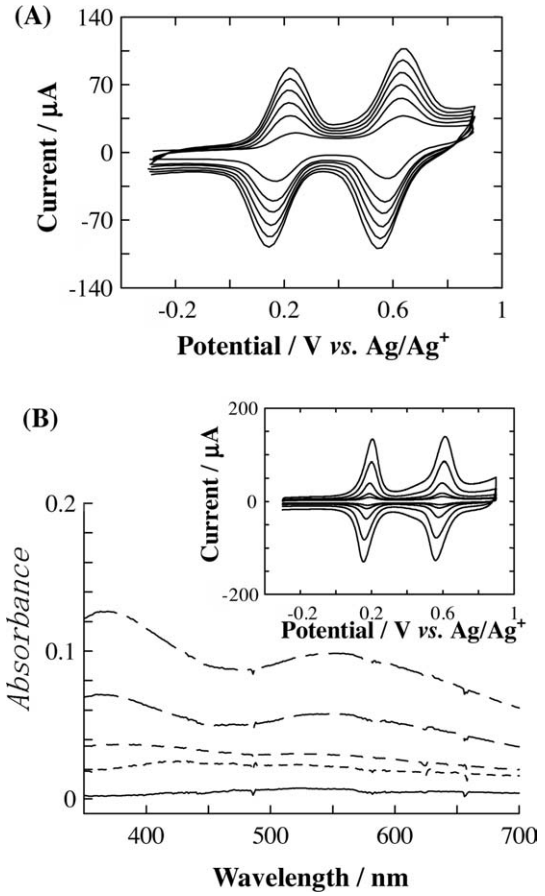

Fig. 3. (**A**) Cyclic voltammograms of 1.7 μM of **3** at ITO in 0.1 M Bu_4NClO_4–CH_2Cl_2 at 100 mV s^{-1} between –0.3 and 0.9 V vs. Ag/Ag^+ in the positive direction at the 1st, 10th, 20th, 30th, 40th, and 50th cyclic scans, as shown from the bottom of the figures to the top. (**B**) UV–Vis spectra and (inset) cyclic voltammograms in 0.1 M Bu_4NClO_4–CH_2Cl_2 of electrodeposited Au_n-BFc films of 3 prepared under the same conditions as those for Fig. 3A with 3, 10, 25, 50, and 75 cyclic scans, as shown from the bottom of the figure to its top.

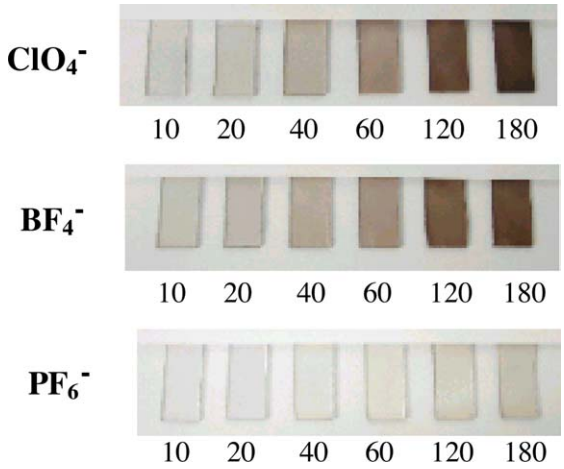

Fig. 4. Photographs of electrodeposited Au_n-BFc films prepared in a solution of 5.0 μM of **2** (θ_{BFc} = 15) at ITO in CH_2Cl_2 with 0.1 M tetra-*n*-butyl ammonium salt of the anion given in the Fig. at ITO at 100 mV s^{-1} between –0.3 and 0.9 V vs. Ag/Ag^+. The numbers in the figure are those of the cyclic scans.

tional to the potential scan rate (not shown in the figure), indicating the behavior of surface-immobilized BFc species in the film where the Au_n-BFc particles are tightly assembled on an electrode.

The film formation of **1, 2, 4** and **5** occurring similar to as described above is easily possible; the construction of Au_n-BFc films with different core diameters is possible when using this electrodeposition process, independent of the core size. It should be noted that in UV–Vis spectra, the Au_n-BFc film, except for **1,** exhibits a broad absorption band at ca. 550 nm that is due to the collective SP band influenced by the dipole–dipole coupling among the adjacent particles (see below) [30].

The current growth induced by cyclic potential scans is also positive when another tetrabutylammonium salt with a different anion, Bu_4NBF_4 or Bu_4NPF_6, is adopted; however, its increasing rate depends on the anion. As displayed in Fig. 4, the color change of the Au_n-BFc films on ITO evidently confirms this difference in electrodeposition rates, in the order of $ClO_4^- \sim BF_4^- >> PF_6^-$ [18]. The Au_n-BFc film could be fabricated in other organic solvents, e.g. THF and toluene/acetonitrile (2:1 v/v), that dissolve Au_n-Bfc and that remain stable within the potential range of electrolysis for Au_n-BFc.

2.1.2. Pd_n-BFc

The preparation of Pd_n-BFc [25] was performed by an exchange reaction of octyl thiolate-covered Pd nanoparticles (Pd_n-OT, d_{av} = 3.8 nm) with BFcS in CH_2Cl_2. A convenient method was employed to synthesize Pd_n-OT [31]. In one liquid phase of THF, the starting Pd complex was reduced by super hydride with a stabilizer of alkylammonium bromide to form naked Pd nanoparticles, with the continuous addition of excess octanethiol by exchange of the surface stabilizer (Scheme 2). The number of Pd core atoms and octyl thiolate molecules on the Pd surface in Pd_n-OT is

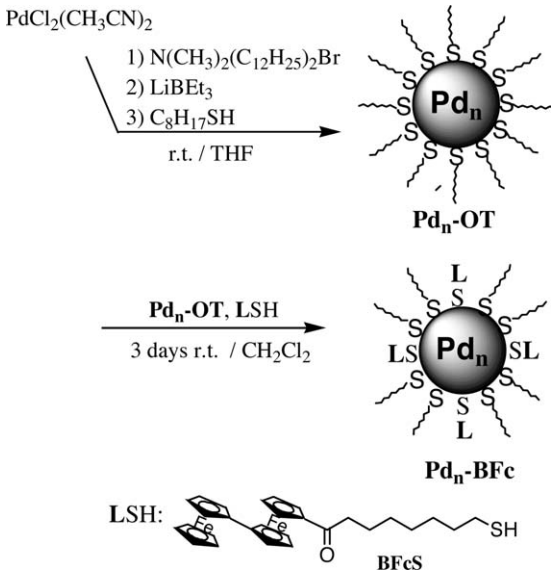

Scheme 2. Preparation of Pd_n-OT and Pd_n-BFc.

estimated to be 2406 atoms and 326 molecules, respectively. The UV-Vis spectrum of Pd_n-BFc exhibits an exponential-decay Mie-scattering spectrum, just as in Pd_n-OT, as well as a small shoulder due to the d-d transition of the BFc moiety at 462 nm (ε_{max} = 9.1 × 10^2 $M^{-1}cm^{-1}$).

Cyclic voltammograms of Pd_n-BFc at a 3-mm diameter glassy carbon (GC) electrode in Bu_4NClO_4–CH_2Cl_2 show a two-step one-electron oxidation wave at 0.18 and 0.58 V vs. Ag/Ag^+ derived from the BFc moieties, of which both the cathodic and the anodic peak current values for the first-step reaction increase almost linearly to the potential scan rate with the small value of the peak-to-peak separation (34 mV). The value of the cathodic peak current exceeds the anodic value after the second-step reaction, providing additional evidence that the two-electron oxidation of the biferrocene units triggers the electro-oxidative deposition of Pd_n-BFc on the electrode. Actually, consecutive potential scans using ITO as a working electrode produce a gradual increase in the peak current, to construct an adhesive Pd nanoparticle film. The UV–Vis spectrum and cyclic voltammograms of the electrodeposited films prepared with different numbers of consecutive scans show that the film layers develop with an increase in the number of potential scans (Fig. 5), resembling the case of Au_n-BFc.

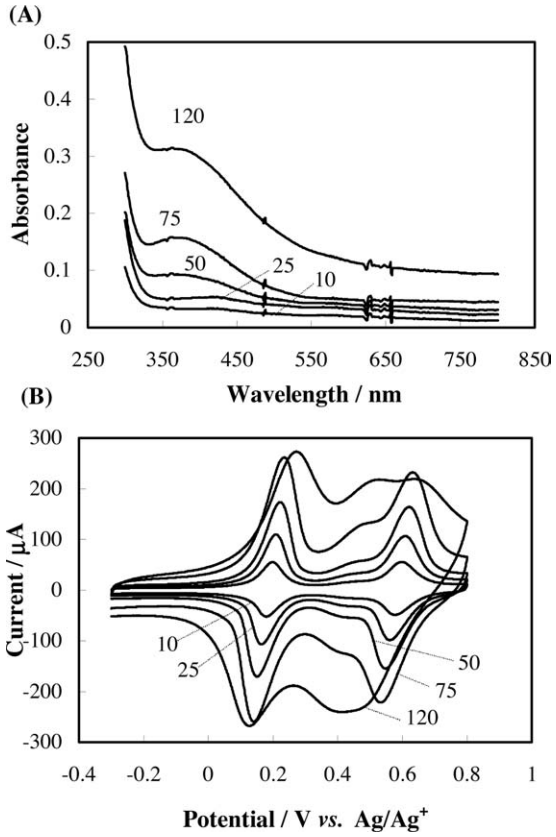

Fig. 5. (**A**) UV-Vis spectra and (**B**) cyclic voltammograms of electrodeposited Pd_n-BFc films prepared in a solution of 1.9 μM Pd_n-BFc with consecutive potential scans at ITO in 0.1 M Bu_4NClO_4–CH_2Cl_2 at 100 mV s^{-1} between –0.3 and 0.9 V vs. Ag/Ag^+ in the positive direction. Numbers in the figure refer to those of cyclic scans.

2.1.3. An alternating multi-layered structure of Au_n-BFc and Pd_n-BFc

A combination of electro-oxidative deposition of Au_n-BFc and Pd_n-BFc forms a thin BFc-active composite film with a layered hybrid structure (Scheme 3) [32]. First, the electrodeposition of Pd_n-BFc is performed by potential cyclic scans between –0.3 and 0.9 V for the redox reaction of Pd_n-BFc, which is followed by the electrodeposition of **3** under the same conditions as those for the formation of the Pd_n-BFc film, thus forming the Pd_n-BFc/Au_n-BFc composite film. The two-step hetero-electrodeposition procedure is repeated to increase the number of composite layers. A UV–Vis spectrum of the film thus prepared shows broad absorption bands that grow in intensity with increases in the number of composite layers (Fig. 6A). The cyclic voltammogram of the film in a pure electro-

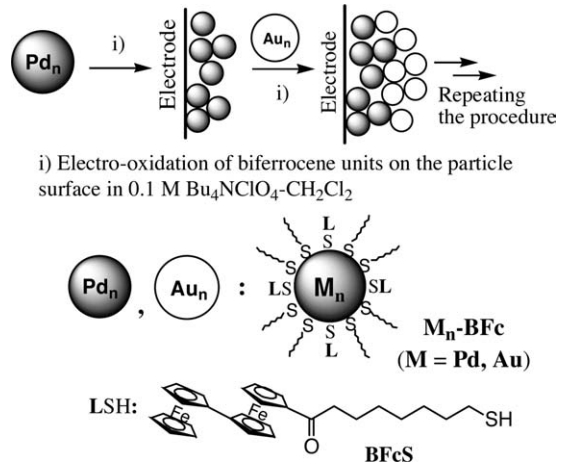

Scheme 3. Preparation of Pd_n-BFc and Au_n-BFc composite film.

lyte solution exhibits two redox waves at $E^{0'} = 0.18$ V for BFc^+/BFc, and at 0.58 V for BFc^{2+}/BFc^+, as shown in the inset of Fig. 6A, in which the amount of charge for the two redox waves increases with an increase in the number of composite layers. Fig. 6B shows the XPS spectra of the composite film using the C 1s peak (284.5 eV) as a reference. The Au $4f_{5/2}$ (87.5 eV) and $4f_{7/2}$ (83.9 eV) peaks [33] are not detected in the first layer of Pd_n-BFc, although they appear after deposition of the second layer of Au_n-BFc. In addition, formation of the third layer of Pd_n-BFc shelters most of these peaks, suggesting that the prepared films build up an alternately layered structure of Pd_n-BFc and Au_n-BFc. These results demonstrate that sufficient electron transfer exists among heterogeneous interfaces of Pd_n-BFc and Au_n-BFc to develop the composite film, accumulating average 5 M_n-BFc (M = Pd, Au) layers above the second layer.

2.2. Electro-reductive deposition process of Au_n-AQ

Au_n-AQ ($\varepsilon_{max} = 7.7 \times 10^5$ M^{-1} cm^{-1} at 516 nm of the SP band; $\varepsilon_{max} = 9.1 \times 10^5$ M^{-1} cm^{-1} at 444 nm, $\varepsilon_{max} = 1.3 \times 10^6$ M^{-1} cm^{-1} at 316 nm of AQ sites) was synthesized by a substitution reaction between AQS and Au_n-AT and was used for the preparation of **2**. The number of exchanged AQ-terminated thiolates on the Au_n-AT surface, θ_{AQ}, was determined by the ratio of the integrals of ^{1}H-NMR signals between AQ and methyl protons at ca. 7.5 and 1.0 ppm, respectively. Cyclic voltammograms for the electrodeposition process of Au_n-AQ ($\theta_{AQ} = 26$) in Bu_4NClO_4-toluene/acetonitrile

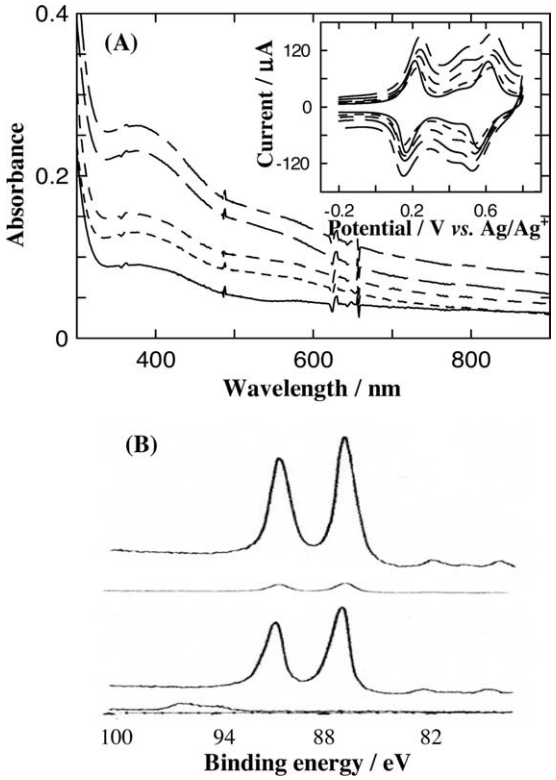

Fig. 6. (**A**) The UV–Vis spectrum, (inset) the cyclic voltammogram, and (B) the XPS spectrum of Pd_n-BFc, Pd_n-BFc/Au_n-BFc, Pd_n-BFc/Au_n-BFc/Pd_n-BFc, [Pd_n-BFc/Au_n-BFc]$_2$, [Pd_n-BFc/Au_n-BFc]$_2$$Pd_n$-BFc (for Fig. 6A. only) films, as shown from the bottom of the figure to its top. The films were prepared with 25 cyclic potential scans between –0.3 and 0.9 V vs. Ag/Ag^+ for each metal nanoparticle film in a solution of 3.2 μM Pd_n-BFc, or Au_n-BFc, at ITO in 0.1 M Bu_4NClO_4–CH_2Cl_2 at 100 mV s^{-1}.

(2:1 v/v) at ITO are shown in Fig. 7. Consecutive potential scans between –1.0 and –2.0 V vs. Ag/Ag^+, where two-electron reduction of AQ units occurs, exhibit a gradual increase in the peak current to form redox-active gold nanoparticle films. Note that the appearance of only one redox wave is derived from the existence of considerable interaction between the hydroxide groups of the ITO base. UV–Vis spectra of the prepared Au_n-AQ films show broad absorption bands with a particle-particle interaction (see above) that grows in intensity with increases in the number of potential scans (Fig. 8A). The cyclic voltammogram of the electrodeposited Au_n-AQ film prepared with 10 potential scans in Fig. 8A exhibits a redox reaction of adsorbed species at –1.26 and –1.81 V vs. Ag/Ag^+ (Fig. 8B). Electrochemical analysis using a microelec-

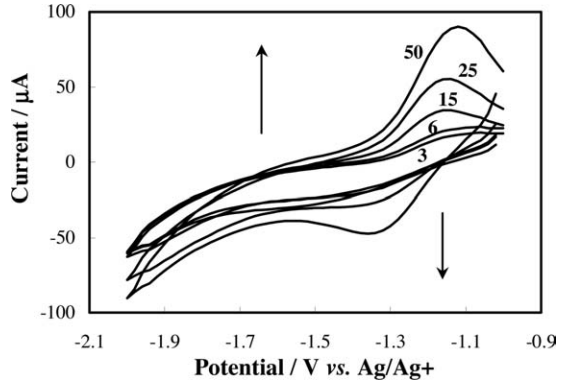

Fig. 7. Cyclic voltammograms of 6.2 μM Au_n-AQ (θ_{AQ} = 26) at ITO in 0.1 M Bu_4NClO_4–toluene/acetonitrile (2:1 v/v) at 100 mV s^{-1} between –1.0 and –2.0 V vs. Ag/Ag^+ in the negative direction. Numbers in the figure refer to those of cyclic scans.

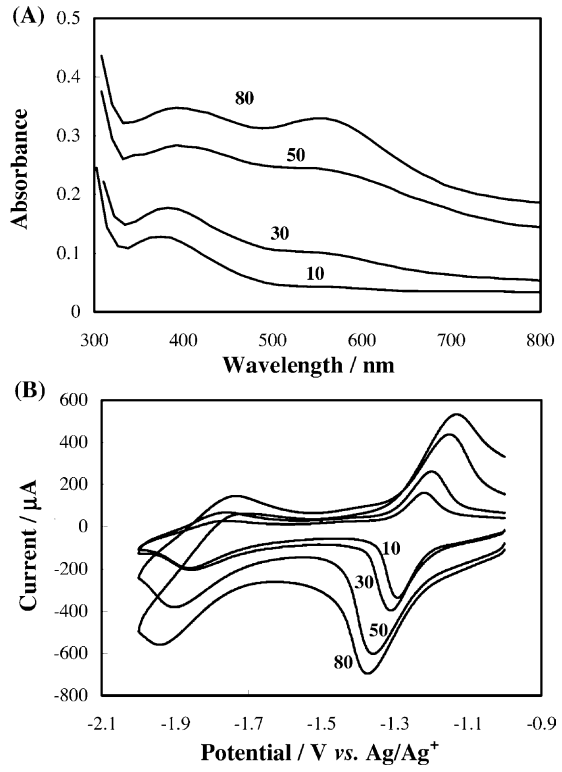

Fig. 8. (**A**) UV–Vis spectra and (**B**) cyclic voltammograms of the electrodeposited Au_n-AQ films prepared in a solution of 6.3 μM Au_n-AQ (θ_{AQ} = 26) with consecutive potential scans at ITO in 0.1 M Bu_4NClO_4–CH_2Cl_2 at 100 mV s^{-1} between –1.0 and –2.0 V vs. Ag/Ag^+ in the negative direction. Numbers in the figure refer to those of cyclic scans.

trode [34] has demonstrated that the double-layer charging capacitance of Au_n-AQ, $C_{dl,Au}$, relating to the slope of $\Delta I/\Delta E$ in cyclic voltammograms, increases with the accumulation of negative charge on the AQ moiety; namely, $C_{dl,Au}$ (AQ) < $C_{dl,Au}$ ($AQ^{\bullet-}$) < $C_{dl,Au}$ (AQ^{2-}) [20, 21].

2.3. Basic morphological aspects of the electrodeposited M_n-BFc (M = Au, Pd) and Au_n-AQ films

The specific morphological features of the M_n-BFc (M = Au, Pd) and Au_n-AQ films were determined by scanning tunneling microscopy (STM) and atomic force microscopy (AFM). The changes in surface structure in response to increases in the number of potential scans in the electrodeposition process are shown in Fig. 9A and B, with STM images of the Au_n-BFc of **2** (θ_{BFc} = 3.6) films at a highly oriented pyrolytic graphite (HOPG) deposited in a ClO_4^- solution by 5 and 60 cyclic scans. The spherical Au_n-BFcs gather to construct an island of particles in Fig. 9A, but the whole electrode area is not covered and the clear step-line of the HOPG surface still appears when the number of potential scans is five. By 60 potential scans in Fig. 9B, the Au_n-BFcs of a similar size are tightly assembled to cover the entire electrode surface and to build up multiple layers with a fairly flat surface.

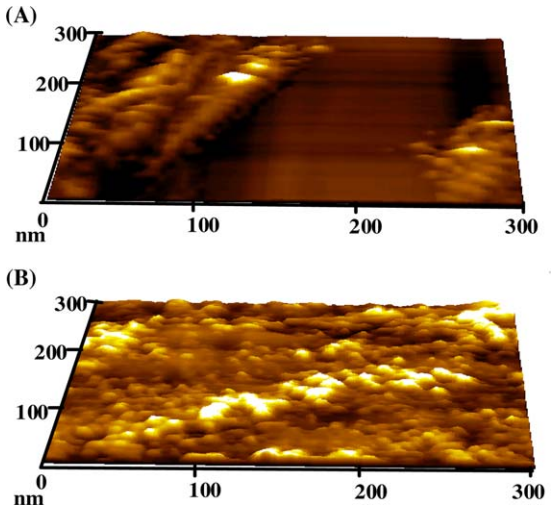

Fig. 9. The STM image of the Au_n-BFc film prepared in a solution of 5.3 μM of **2** (θ_{BFc} = 3.6) at HOPG with (**A**) 5 and (**B**) 60 cyclic potential scans in 0.1 M Bu_4NClO_4–CH_2Cl_2 at 100 mV s^{-1} between –0.3 and 0.9 V vs. Ag/Ag^+ in the positive direction.

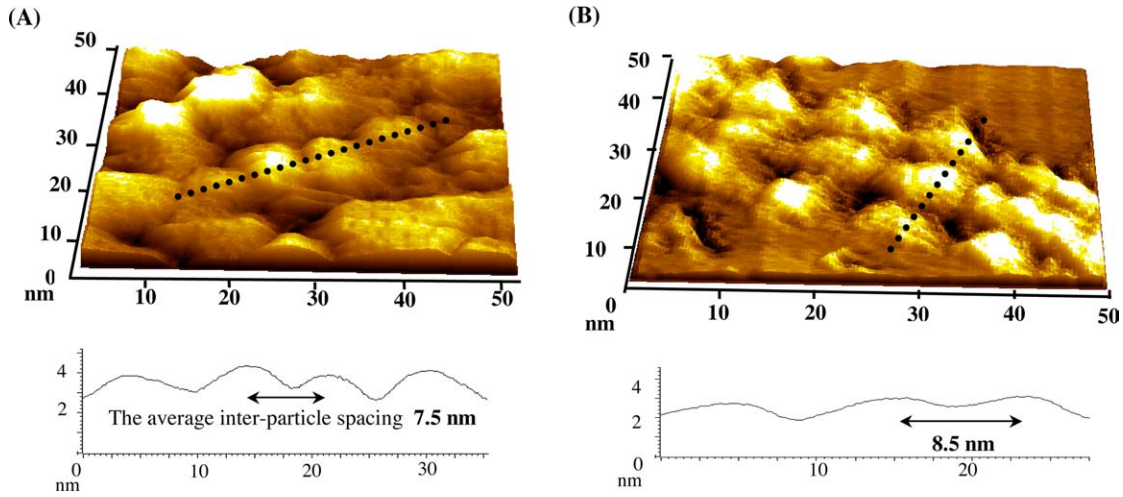

Fig. 10. The enlarged STM image of the (**A**) Au_n-BFc of **2** (θ_{BFc} = 3.6) and (**B**) Au_n-AQ (θ_{AQ} = 26) film (top), and the cross-sectional profile along the dotted line (bottom).

Fig. 10A is the enlarged image of Fig. 9B, and shows that the average spacing between the adjoining electrodeposited Au_n-BFcs is 7.5 nm. This value is obviously larger than the estimated maximal Au_n-BFc particle size of 5.9 nm (core diameter, 2.3 nm; octyl thiolate, 1.0 nm; and BFc, 0.8 nm), even if a deviation in core diameter of 0.5 nm is taken into consideration. The Au_n-AQ film of Fig. 10B also suggests that the practical inter-particle spacing is measured as 8.5 nm, which is much larger than the estimated maximal Au_n-AQ value of 5.9 nm (the core diameter, 2.3 nm; octyl thiolate, 1.0 nm; and AQ, 0.8 nm), indicating the existence of spacing between the Au_n-Aqs, the same as in Au_n-BFcs. Moreover, it is noticeable that Au_n-AQ particles are closely packed to form a tetragonal-like array, which is seen in the film of **3** [19] and Pd_n-BFc (see below).

STM and AFM images of the Au_n-BFc film (θ_{BFc} = 7.5) are shown in Fig. 11A and B. The surface in Fig. 11A maintains a monolayer-level flatness seen in its cross-sectional view, whereas it is apparent that domains of particles ca. 70–80 nm in diameter (encircled by a dotted line) are constructed. The AFM image of the same sample reveals this peculiar nanostructure of the Au_n-BFc film; round-shaped domains spreading across the whole surface are shown in Fig. 11B.

This disagreement with regard to the interparticle distance, the particle domain structure, and the tetragonal-like aggregation were also observed for the Pd_n-BFc films (Fig. 12), indicating that these characteristics in assembled structures generally emerge in this deposition system.

3. Electrodeposition mechanism of Au_n-BFc

3.1. Consideration of the electrolyte dependence and STM images

In this section, our basic interest in mechanistic analysis of this system should be noted, especially concerning Au_n-BFc. Possible candidates for the driving force of this electrochemical aggregation are ‘physical interactions’ and/or ‘chemical bond formation’ among the particles (Fig. 13). The former would be attributed to the collective interaction among the charged Au_n-BFc, electrolyte and solvent in solution, while the latter could be defined as the coupling reaction of the BFc units on the neighboring nanoparticles, which could occur when they are oxidized to become reactive [35]; however, ‘physical interaction’ is convincingly supported first by ‘the anion effect’ for the electrodeposition rate of Au_n-BFc (Fig. 4). Assuming that anions surround the BFc units on the Au_n-BFc surface, acting as a counterion in the electrooxidation process, the charged Au_n-BFcs and the counter anions are likely to assemble voluntarily as a result of their lattice energy, which involves electrostatic force and to

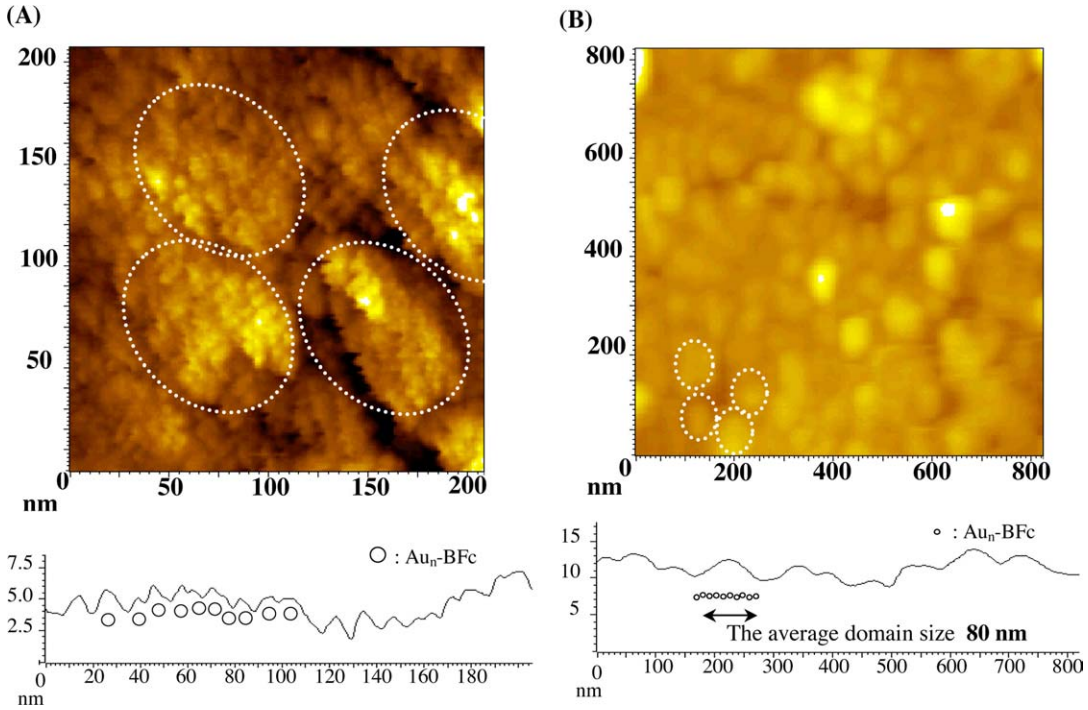

Fig. 11. The STM (A, top) and AFM (B, top) images of the Au$_n$-BFc film prepared in a solution of 5.2 μM **2** (θ_{BFc} = 7.5) at HOPG with five cyclic scans in 0.1 M Bu_4NClO_4–CH_2Cl_2 at 100 mV s^{-1} between –0.3 and 0.9 V vs. Ag/Ag^+ in the positive direction, and the typical cross-sectional profile along the cross axis (bottom).

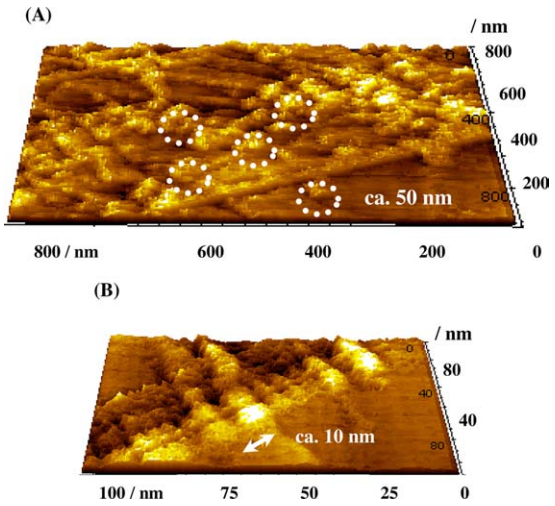

Fig. 12. The STM image of the Pd$_n$-BFc film prepared in a solution of 1.9 μM Pd$_n$-BFc at HOPG with 60 cyclic scans in 0.1 M Bu_4NClO_4–CH_2Cl_2 at 100 mV s^{-1} between –0.3 and 0.9 V vs. Ag/Ag^+ in the area of (**A**) 800 × 800 nm^2 and (**B**) 100 × 100 nm^2.

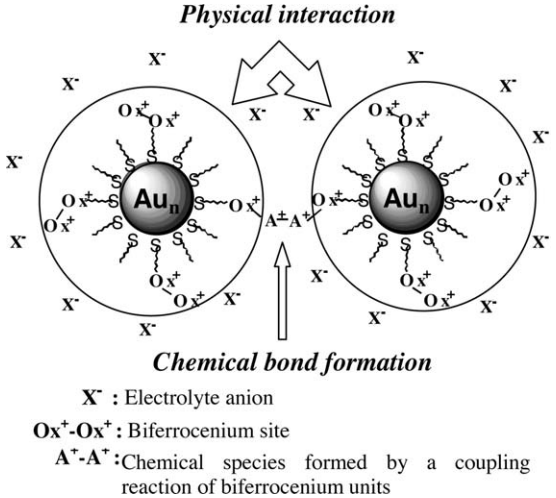

Fig. 13. Two possible mechanisms of electrodeposition between adjacent Au$_n$-BFc particles by electro-oxidation.

some extent van der Waals-like force. Hence, when the particles cannot get closer to each other with the larger anions, the electrodeposition proceeds less efficiently with a smaller attractive van der Waals-like force. The

diameter of PF_6^-, 3.3 Å, is significantly larger than that of the other anions (ClO_4^-: 2.3 Å, BF_4^-: 2.1 Å), which accords well with the experimental results regarding the deposition rate (see above).

Second, the possibility of a deposition mechanism involving 'chemical bond formation' can be excluded, considering the finding on the STM image (Fig. 10A) that the Au_n-BFcs are not electrodeposited via direct contact between BFc moieties and/or the alkyl chain with maintaining a certain distance between the particles. The most likely candidate for the chemical species existing in the space among adjacent Au_n-BFcs in the film, estimated at 7.5–5.9 = 1.6 nm, is the electrolyte being used, even if the potential in the electrodeposition experiment is stopped at –0.3 V, at which point BFc units are in the neutral state. Practically, the presence of anions and the proportion of Au_n-BFc particles and BF_4^- anions in the film prepared in BF_4^- solution were evidenced by the prompt γ-ray neutron activation analysis (PGA) method [36, 37] and by inductively coupled plasma (ICP), which gave the ratio of the Au_n-BFc (θ_{BFc} = 7.5) particle and BF_4^- anion in the film as 1 to 9.3. This value allows us to estimate that 62 % of the counter anions of BFc^{2+} remain as spacers.

3.2. Deposition dynamics of Au_n-BFc

Fig. 14 displays the electrochemical quartz crystal microbalance (EQCM) behavior of **2** (θ_{BFc} = 7.5) at a gold electrode in Bu_4NClO_4–CH_2Cl_2. In the first potential sweep in the positive direction, only a slight frequency decrease is observed in the first electron oxidation of the BFc moieties at $E^{0\prime}{}_1 = 0.15$ V, whereas the frequency decreases dramatically from 0.54 to 0.9 V when the second electron oxidation of the BFc sites takes place at $E^{0\prime}{}_2 = 0.54$ V. This behavior reflects the conclusive electro-oxidative aggregation of Au_n-BFcs occurring with the 2-e^- oxidation of the BFc units, since a frequency decrease relates to a mass increase on the electrode. The changed mass weight on an electrode is calculated by the Sauerbery equation ($\Delta F = -C \times \Delta W$, where ΔF is the frequency change, C is the proportional constant that depends on the parameters of QCM electrode properties – e.g., the electrode area, quartz density, and quartz elasticity, and the value is equivalent to 6.17×10^7 Hz g^{-1} in this study), and ΔW is the weight change on the electrode.

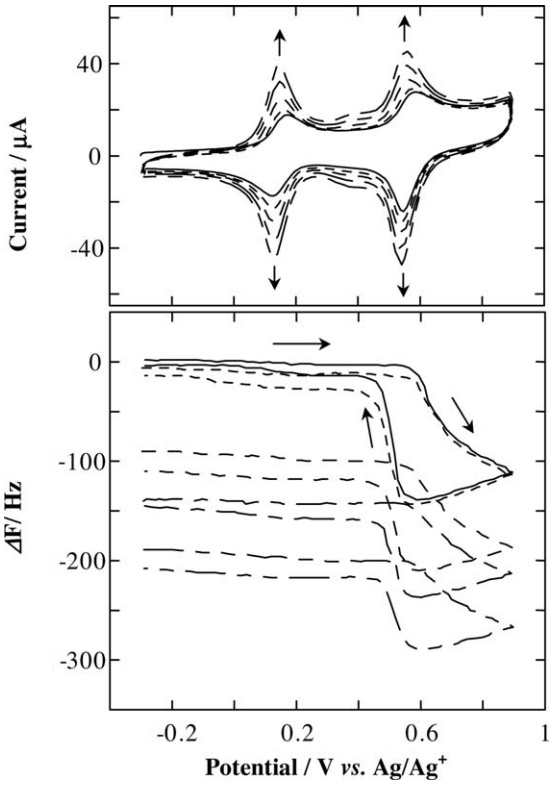

Fig. 14. Cyclic voltammograms (top) and ΔF-potential curves (bottom) of 5.2 μM of **2** (θ_{BFc} = 7.5) at a gold electrode in 0.1 M Bu_4NClO_4–CH_2Cl_2 at 100 mV s^{-1} between –0.3 and 0.9 V vs. Ag/Ag^+ in the positive direction with the 1st (solid line), 5th (dotted line), 10th (dashed line), 15th (dot-dashed line), and 20th (2-dot-dashed line) scans.

When the potential scan is reversed at 0.9 V to the negative potential, the frequency continues to decrease until 0.54 V; however, a significant frequency increase starts after the electrode potential becomes more negative than $E^{0\prime}{}_2$. Thus, the frequency difference, ΔF, before and after the potential cycling at –0.3 V corresponds to the net weight of the deposited Au_n-BFcs. During the course of repeated cyclic potential scans, the frequency steadily decreased after each cycle with current increases of the cyclic voltammograms, corresponding to a continuous accumulation of the Au_n-BFc layer on the electrode surface. These results indicate the following electrodeposition dynamics of Au_n-Bfc, as summarized in Fig. 15: (1) Au_n-BFcs are apt to aggregate at the electrode/electrolyte interface and to adsorb to the electrode by formation of the BFc^{2+} state

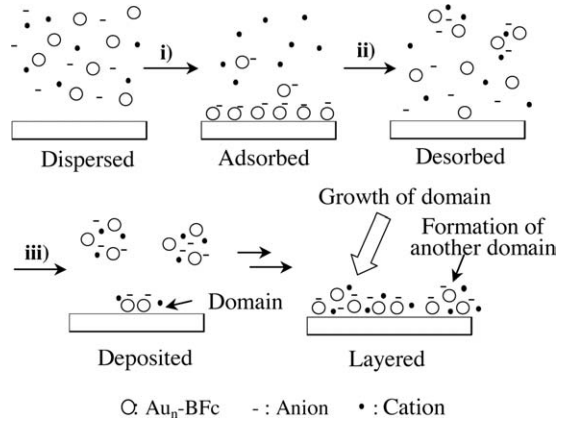

Fig. 15. Illustration of the electrodeposition process in Au$_n$-BFc solution at the electrode interface. (*i*) Two-electron oxidation of the BFc sites, (*ii*) set back to the neutral state by two-electron reduction, and (*iii*) repeating the potential sweep.

on the particle surface; (2) significant desorption of assembled Au$_n$-BFcs from the electrode occurs after BFc sites are returned to the neutral state by reduction; and (3) a small portion of the strongly adsorbed flocks of Au$_n$-BFcs remain on the electrode. By repeating the potential scans, the Au$_n$-BFc film might be fabricated by the remaining adsorbed Au$_n$-BFcs, resulting in formation of the domains demonstrated in the STM and AFM images.

EQCM measurement of the Au$_n$-BFc film itself in Bu_4NClO_4–CH_2Cl_2 provides insight into the movement of electrolyte ions in the redox process of the film [18]. Namely, the second oxidation of the BFc moieties in the Au$_n$-BFc film triggers an increase in the local ionic interaction with the anions and increases polarity around the particles; subsequently, the solvent molecules of CH_2Cl_2 are naturally expelled from the charged Au$_n$-BFc film. A simplified picture of chemical species motion for the two-step redox reaction of Au$_n$-BFc in the film is shown in Fig. 16. It is expected that the porous Au$_n$-BFc film with long inter-particle spacing acts like a nano-sponge, and the solvent molecules, anions in the solution, and possibly pre-included cations move into and out from the film reversibly at $E_2^{0\prime}$ by changing the electronic charge of the BFc sites (Fig 16, *ii*)). Note that the exclusion of solvent is not observed at $E_1^{0\prime}$ in accord with the electrodeposition phenomenon of Au$_n$-BFcs. It can be inferred that the exclusion of solvent molecules around

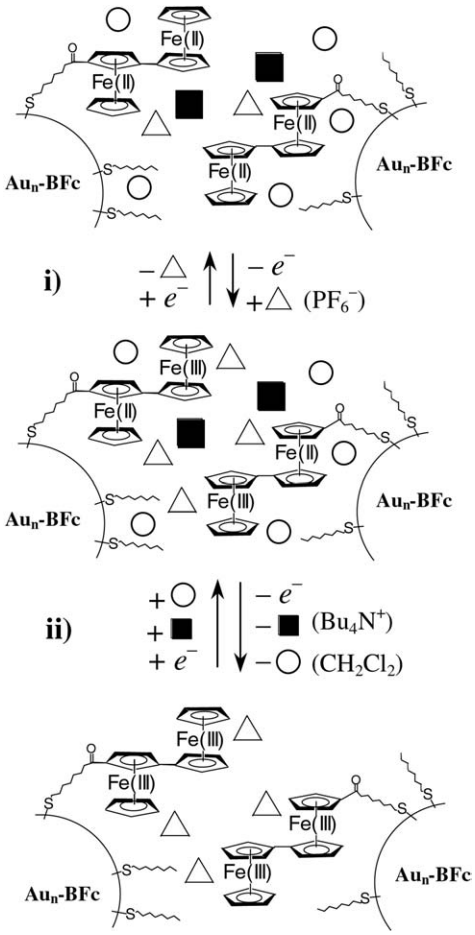

Fig. 16. The illustration of ion motion for the two-step redox reaction of Au$_n$-BFc in the film. The first (*i*) and the second (*ii*) redox reaction of the BFc sites in the film.

Au$_n$-BFcs at $E_2^{0\prime}$ causes additional inter-particle approaching and precipitation, thus effectively forming an ionic lattice including Au$_n$-BFc^{2+} and counterion.

4. Nature of the formed film with regard to interparticle interactions

4.1. Solvent refractive index effects on surface plasmon absorption of the Au$_n$-BFc film

The electrodeposited Au$_n$-BFc film with a collective SP band is interesting to investigate with regard to the optical properties of metal nanoparticles compared with those of individual particles in solution. The SP

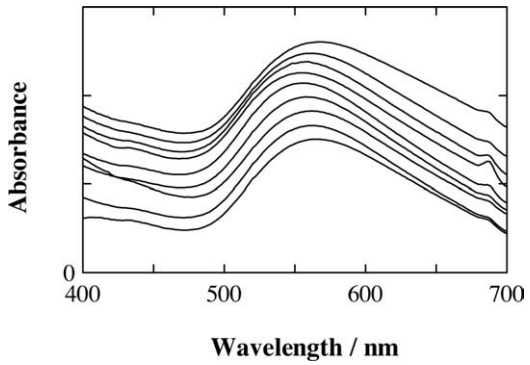

Fig. 17. UV–Vis spectra of the thin Au_n-BFc film ($\Gamma_{BFc} = 6.0 \times 10^{-11}$ mol cm^{-2} = 5 layers) of **2** (θ_{BFc} = 15) on ITO in various solvents. Each spectrum was measured from the top to the bottom in water ($n_d^{20} = 1.33$), acetonitrile ($n_d^{20} = 1.34$), acetone ($n_d^{20} = 1.36$), ethanol (n_d^{20} = 1.36), dichloromethane (n_d^{20} = 1.42), chloroform (n_d^{20} = 1.44), benzene (n_d^{20} = 1.50), *o*-dichlorobenzene ($n_d^{20} = 1.55$), and carbon disulfide ($n_d^{20} = 1.62$).

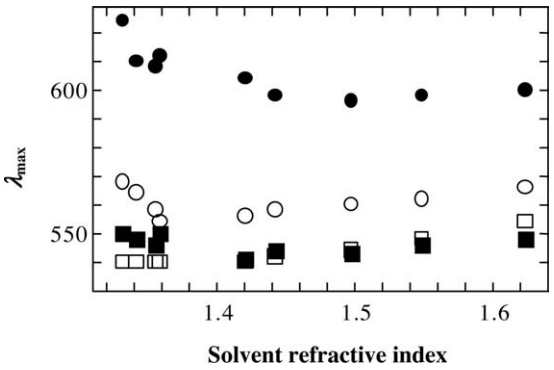

Fig. 18. Plots of the absorption maximum (λ_{max}) of the Au_n-BFc film [closed circles: **2** (thick: $\Gamma_{BFc} = 1.9 \times 10^{-10}$ mol cm^{-2} = 18 layers), open circles: **2** (thin: $\Gamma_{BFc} = 6.0 \times 10^{-11}$ mol cm^{-2} = 5 layers), closed squares: **4** (thick: $\Gamma_{BFc} = 4.5 \times 10^{-11}$ mol cm^{-2} = 16 layers), open squares: **4** (thin: $\Gamma_{BFc} = 1.3 \times 10^{-11}$ mol cm^{-2} = 5 layers) vs. the solvent refractive index.

band of noble metal sols (almost 'naked' particles) is quite sensitive to the electronic environment around metal particles, including the refractive index of the solvent medium [21, 38, 39], as predicted by Mie theory [40]; recently, Mulvaney et al. [41] have explained the influence of the solvent refractive index on the SP band for alkyl thiolate-attached gold particles, considering the shelter effect of the alkyl thiolate chain, concluding that the values for the gold nanoparticle's plasmon wavelengths (λ_{max}) are linear to those of the solvent refractive index, n_d^{20}. The UV-Vis spectral changes of the Au_n-BFc film of **2** (θ_{BFc} = 15) are shown in Fig. 17 as a function of the solvent refractive index from n_d^{20} = 1.33 (top) to n_d^{20} = 1.62 (bottom). Note that the values for Au_n-BFc coverage on an electrode, Γ_{BFc}, refer to the figure legends. Γ_{BFc} can be estimated from the optical measurements by equation: $\Gamma_{BFc} = A/1000\,\varepsilon$ [mol cm^{-2}], where A is the absorbance at the SP band and ε is the molar extinction coefficient at the SP band for each particle. The number of layers is estimated by assuming that the electrodeposited nanoparticles are hexagonally packed in the film.

The absorbance is normalized for easy recognition of the spectral shift. The SP band maximum at 569 nm in water (n_d^{20} = 1.33) gradually shifts to higher energy with increases in the refractive index value until it reaches 557 nm in dichloromethane (n_d^{20} = 1.42); it then moves towards lower energy until it reaches 567 nm in carbon disulfide, where it has the largest refractive index value, n_d^{20} = 1.62.

Fig. 18 displays the plots of λ_{max} of the collective SP band position vs. solvent refractive index values for each Au_n-BFc film of **2** and **4**, suggesting that the values of λ_{max} are not proportional to those of n_d^{20}, having a clear V-shaped curve, and the shifts are much larger, especially in the region of polar solvents, which is not predicable from the theory of isolated particles. These results can be explained by the observation that the SP band of the closely packed Au_n-BFc film is fairly affected by the particle-particle interaction, not identified as the precise SP band of a single particle, and/or the difference in affinity of the solvents to the non-polar alkyl chain on the particles, which perturbs the solvent-particle core interaction.

4.2. Potential dependence of surface plasmon absorption of the electrodeposited Au_n-BFc film

The alkyl thiolate-covered gold nanoparticles can be electrolytically charged by one-electron oxidation or by reduction with the applied potential [42, 43], and this charging affects the energy of the SP band [21, 41, 44]. The charge influence of the Au_n-BFc film was investigated by observing the spectral changes over shifts in the potential with core-size dependence (Scheme 4).

Fig. 19 shows the spectroelectrochemical data showing the changes with the λ_{max} of the SP band, which is located at 584 nm at the starting potential of 0 V vs. Ag/Ag^+ in Bu_4NClO_4–CH_2Cl_2 for the Au_n-BFc

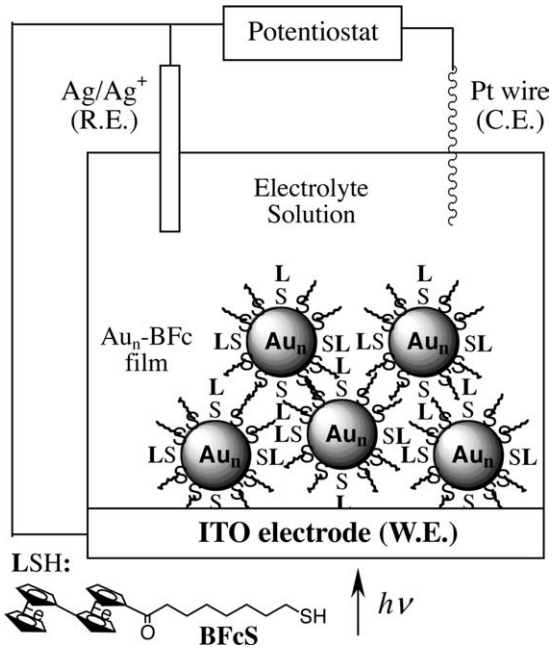

Scheme 4. The spectroelectrochemical cell of the Au_n-BFc film.

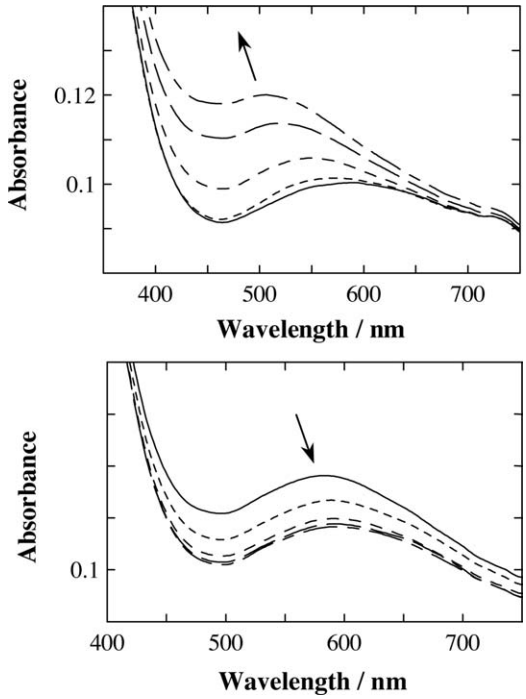

Fig. 19. [Top] UV-Vis spectra of the Au_n-BFc film of **5** (Γ_{BFc} = 1.3 × 10^{-11} mol cm^{-2} = 15 layers) on ITO at given potentials of 0, –0.4, –0.8, –1.2, and –1.6 V vs. Ag/Ag^+ in 0.1 M Bu_4NClO_4–CH_2Cl_2 in the negative direction. [Bottom] UV–Vis spectra of the Au_n-BFc film of 5 on ITO at given potentials of 0, 0.4, 0.8, 1.2, and 1.6 V *vs.* Ag/Ag^+ in 0.1 M Bu_4NClO_4–CH_2Cl_2 in the positive direction.

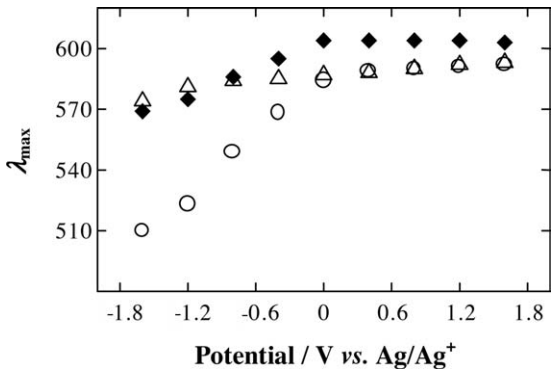

Fig. 20. The plots of the absorption maximum (λ_{max}) of the Au_n-BFc film of **2** (θ_{BFc} = 15: Γ_{BFc} = 1.3 × 10^{-10} mol cm^{-2} = 35 layers) [triangles], **4** (Γ_{BFc} = 4.6 × 10^{-11} mol cm^{-2} = 29 layers) [squares], and **5** (Γ_{BFc} = 1.3 × 10^{-11} mol cm^{-2} = 15 layers) [circles] film vs. the applied potential.

film of **5**. The λ_{max} value is extremely shifted to a shorter wavelength by 74 nm, and the absorbance increases with the potential shift in the negative direction to –1.6 V. The positive potential shift from 0 to 1.6 V gives a longer λ_{max} by 8 nm and a lower absorbance. These spectral changes indicate that the direct charging of the metal core is predominant compared to the charge accumulation at the terminal BFc units because the shift in the negative potential is significantly larger than that in the positive direction where redox reaction of BFc moieties could occur. This finding is in agreement with observations of the film of AQ-attached gold nanoparticles [21].

Regarding the prepared Au_n-BFc films of **2** (θ_{BFc} = 15), **4**, and **5**, the values of λ_{max} are plotted vs. those of applied potential in Fig. 20. There it is noticeable that the shift of λ_{max} is more conspicuous for the Au_n-BFc film with larger core size in the negative potential region. The electroscopic data are summarized in Table 2 and suggest that the particle–particle interaction works more effectively in the Au_n-BFc film with larger particle size, with consideration that the shifts grow with increases in the core size of particles (13 nm for **2**, 35 nm for **4**, and 74 nm for **5**). It is interesting that the order of the ideal λ_{max} shift is in opposition to the experimental values; namely, the theoretical equations noted above predict that the SP band position of the isolated particles is stimulated more easily by applied potential with a smaller core

Table 2
Spectroelectrochemical data of the Au_n-BFc films

Compound	C_{core}[a] (aF)	ΔV[b] (V)	Number of injected electrons to the core[c]	λ_{init}[d] (nm)	λ_{final}[d] (nm)	$\lambda_{final.ideal}$[e] (nm)	$\Delta\lambda_{ex}$[f] (nm)	$\Delta\lambda_{ideal}$[g] (nm)
2	1.1	0.15	11 e^-	587	574	577	13	10
4	2.8	0.057	28 e^-	604	569	601	35	3
5	4.2	0.038	42 e^-	584	510	582	74	2

[a] The core capacitance: $C_{core} = 4\pi\varepsilon\varepsilon_0 r(r+d)/d$, where ε is the monolayer dielectric constant, r is the core radius, and d is the monolayer thickness.

[b] The potential spacing of consecutive single-electron transfer processes: $\Delta V = e/C_{core}$.

[c] Electron provision from 0 to –1.6 V calculated by the value of ΔV.

[d] See Fig. 20 at 0 V (λ_{init}) and –1.6 V (λ_{final}).

[e] The value calculated by $\lambda_{final.ideal}/\lambda_{init} = (N_{init}/N_{final})^{1/2}$, where N_{init} and N_{final} are the numbers of free electrons per metal core after and before the charging, respectively., referred to Table 1.

[f] $\Delta\lambda_{ex} = \lambda_{init} - \lambda_{final}$.

[g] $\Delta\lambda_{ideal} = \lambda_{init} - \lambda_{final.ideal}$.

size. These results indicate that the collective SP band might be more shifted with interparticle interactions than with a single particle and/or some other parameters affecting the SP resonance; e.g. the electronic state of the surface ligands [29], chemical adsorbates on the surface [45], and the number of layers should be considered for the electrooptical shift [46]. The larger shift in the negative direction might also be ascribed to the difference in the surrounded counter ion affecting the electronic state around the core surface (cations in the negative direction; anions in the positive one) and/or the significant damping of λ_{max} intensity in the positive direction.

4.3. Electrochemical behavior of the Pd_n-BFc/Au_n-BFc composite film

The peculiar electrochemical properties of the Pd_n-BFc/Au_n-BFc film on the ITO electrode were observed in H_2SO_4 aq. by cyclic voltammograms, and the results are displayed in Fig. 21. The sole Pd_n-BFc film undergoes a redox process, exhibiting an oxidation peak at ca. 1.3 V corresponding to the formation of a palladium oxide layer on the particle surface, followed by re-reduction at 0.3 V [47]; the sole Au_n-BFc film possesses the same type of oxidation and reduction peaks at ca. 1.6 and 0.8 V, respectively. In comparison with the cyclic voltammogram of the sole-component films, it is clear that the Pd_n-BFc/Au_n-BFc film exhibits an oxidation peak at ca. 1.3 V, which can be interpreted as the collective oxidation reaction of the Pd_n-BFc and Au_n-BFc. In contrast, the reduction peak appears at ca. 0.3 V, which is the same potential as that of the Pd_n-BFc film, with inhibited reduction of the sole Au_n-BFc

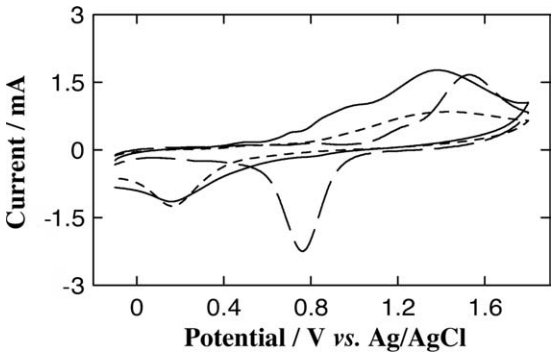

Fig. 21. The cyclic voltammogram of Pd_n-BFc [dots], Au_n-BFc [dashes], and Pd_n-BFc/Au_n-BFc [solid line] films in 0.5 M aq. H_2SO_4 at 100 mV s^{-1}. The films were prepared with 75 cyclic potential scans between –0.3 and 0.9 V vs. Ag/Ag^+ for each metal nanoparticle layer in a solution of 3.2 μM Pd_n-BFc, or Au_n-BFc, in 0.1 M Bu_4NClO_4–CH_2Cl_2 at 100 mV s^{-1} at ITO.

layer at 0.8 V. In addition, the current of the reduction peak is quite small compared to that of the oxidation peaks. No appearance of the peak at 0.8 V suggests that the Pd_n-BFc is sufficiently conductive and capable of mediating the oxidation reaction of Au_n-BFc; however, the electron transfer between the oxidized form of the Pd_n-BFc and Au_n-BFc films is considerably hindered. These results suggest that electron transfer in the metal nanoparticle films can be controlled by changing the combination of core metal elements in this deposition system.

5. Concluding remarks

The present account is concerned with metal nanoparticles functionalized with multiple-redox species,

biferrocene (BFc) and anthraquinone (AQ) derivatives, demonstrating the versatility of metal nanoparticle films, including the construction of heterogeneous Pd-Au nanoparticle composite film, in response to the electrodeposition of M_n-BFc (M = Au, Pd) and Au-AQ with a thickness of up to ~1μm on an electrode by changing some deposition parameters. With various electrochemical, spectroscopic, and mass analyses, a detailed mechanism of electro-oxidative deposition of Au_n-BFc in electrolyte–CH_2Cl_2 solution was elucidated with deposition dynamics. The newly discovered properties derived from the assembled metal nanoparticles were found to be unexplainable by isolated particles alone. These results are important not only with regard to scientific interest in colloid chemistry, but also for the fabrication of metal nanoparticle films, and provide us with basic understanding of the macroscopic properties of assembled nanoparticles that are applicable to optical devices.

Acknowledgements

The present study was supported by Grants-in-Aid for Scientific Research (No. 14204066) and a Grant-in-aid for The 21st-Century COE Program for Frontiers in Fundamental Chemistry from the Ministry of Culture, Education, Science, Sports, and Technology, Japan, and the Research Fellowships of the Japan Society for the Promotion of Science for Young Scientists.

References

[1] J.G.C. Veinot, J. Galloro, L. Pugliese, R. Pestrin, W. Pietro, J. Chem. Mater. 11 (1999) 642.
[2] S.L. Horswell, C.J. Kiely, I.A. O'Neil, D.J. Schiffrin, J. Am. Chem. Soc. 121 (1999) 5573.
[3] A.C. Templeton, S. Chen, S.M. Gross, R.W. Murray, Langmuir 15 (1999) 66.
[4] S. Chen, K. Kimura, Langmuir 15 (1999) 1075.
[5] A.A. Antipov, G.B. Sukhorukov, Y.A. Fedutik, J. Hartmann, M. Giersig, H. Mohwald, Langmuir 18 (2002) 6687.
[6] C. Mangeney, F. Ferrage, I. Aujard, V. Marchi-Artzner, L. Jullien, O. Ouari, E.D. Rekai, A. Laschewsky, I. Vikholm, J.W. Sadowski, J. Am. Chem. Soc. 14 (2002) 5811.
[7] R.B. Little, M.A. El-Sayed, G.W. Bryant, S. Burke, J. Chem. Phys. 114 (2001) 1813.
[8] S.R. Emory, D. Nie, J. Phys. Chem. B 102 (1998) 493.
[9] S. Schauermann, J. Hoffman, V. Johanek, J. Hartmann, J. Libuda, H.J. Freund, Angew. Chem. Int. Ed. Engl. 41 (2002) 2532.
[10] E.R. Leite, N.L.V. Carreno, E. Longo, A. Valentini, L.F.D. Probst, J. Nanosci. Nanotechnol. 2 (2002) 89.
[11] A. Labande, J. Ruiz, D. Astruc, J. Am. Chem. Soc. 124 (2002) 1782.
[12] G. Schmid, M. Bäumle, M. Geerkens, I. Heim, C. Osemann, T. Sawitowski, Chem. Soc. Rev. 28 (1999) 179.
[13] P.V. Kamat, S. Barazzouk, S. Hotchndani, Angew. Chem. Int. Ed. Engl. 41 (2002) 2764.
[14] D.I. Gittins, D. Bethell, D.J. Schiffrin, R.J. Nishols, Nature 408 (2000) 67.
[15] A.C. Templeton, D.E. Cliffel, R.W. Murray, J. Am. Chem. Soc. 121 (1999) 7081.
[16] M. Yamada, A. Kuzume, M. Kurihara, K. Kubo, H. Nishihara, Chem. Commun. (2001) 2476.
[17] T. Horikoshi, M. Itoh, M. Kurihara, K. Kubo, H. Nishihara, J. Electroanal. Chem. 473 (1999) 113.
[18] M. Yamada, T. Tadera, K. Kubo, H. Nishihara, J. Phys. Chem. B 107 (2003) 3703.
[19] M. Yamada, H. Nishihara, Eur. Phys. J. D 24 (2003) 257.
[20] M. Yamada, K. Kubo, H. Nishihara, Chem. Lett. (1999) 1335.
[21] M. Yamada, T. Tadera, K. Kubo, H. Nishihara, Langmuir 17 (2001) 2363.
[22] M.J. Hostetler, S.J. Green, J.J. Stokes, R.W. Murray, J. Am. Chem. Soc. 119 (1997) 9175.
[23] R.S. Ingram, M.J. Hostetler, M.R.W. Murray, J. Am. Chem. Soc. 119 (1997) 9175.
[24] N. Chandrasekharan, P.V. Kamat, Nano Lett. 1 (2001) 67.
[25] M. Yamada, I. Quiros, J. Mizutani, K. Kubo, H. Nishihara, Phys. Chem. Chem. Phys. 3 (2001) 3377.
[26] M. Brust, M. Walker, D. Bethell, D.J. Schiffrin, R. Whyman, J. Chem. Soc., Chem. Commun. (1994) 801.
[27] M.J. Hostetler, J.E. Wingate, C.-J. Zhong, J.E. Harris, R.W. Vochet, M.R. Clark, D. Londono, S.J. Green, J.J. Stokes, G.D. Wignall, M.D. Porter, N.D. Evans, R.W. Murray, Langmuir 14 (1998) 17.
[28] C.M. Lin, C.M. Sorensen, Chem. Mater. 11 (1999) 198.
[29] M.M. Alvarez, J.T. Khoury, T.G. Schaaff, M.N. Shafigullin, I. Vezmar, R.L. Whetten, J. Phys. Chem. B 101 (1997) 3704.
[30] T. Ung, L.M. Liz-Marzan, P. Mulvaney, J. Phys. Chem. B 105 (2001) 3441.
[31] I. Quiros, M. Yamada, K. Kubo, J. Mizutani, M. Kurihara, H. Nishihara, Langmuir 18 (2002) 1413.
[32] M. Yamada, H. Nishihara, Chem. Commun. (2002) 2578.
[33] M.C. Bourg, A. Badia, R.B. Lennox, J. Phys. Chem. B 104 (2000) 6562.
[34] R.S. Ingram, R.W. Murray, Langmuir 14 (1998) 4115.
[35] D. Astruc, Electron-Transfer and Radical Processes in Transition Metal Chemistry, VCH, New York, 1995.
[36] C. Yonezawa, A.K.H. Eood, M. Hoshi, Y. Ito, E. Tachikawa, Nucl. Instr. Meth. Phys. Res. A 329 (1993) 207.
[37] Y. Sakai, C. Yonezawa, M. Magara, H. Sawahata, Y. Ito, Nucl. Instr. Meth. Phys. Res. A 353 (1994) 699.
[38] S. Underwood, P. Mulvaney, Langmuir 10 (1994) 3427.
[39] K.G. Thomas, J. Zajicek, P.V. Kamat, Langmuir 18 (2002) 3722.
[40] G. Mie, Ann. Phys. 25 (1908) 377.

[41] A.C. Templeton, J.J. Pietron, R.W. Murray, P. Mulvaney, J. Phys. Chem. B 104 (2000) 564.
[42] S.W. Chen, R.S. Ingram, M.J. Hostetler, J.J. Pietron, R.W. Murray, T.G. Schaaff, J.T. Khoury, M.M. Alvarez, R.L. Whetten, Science 280 (1998) 2098.
[43] R.P. Andres, T. Bein, M. Dorogi, S. Feng, J.I. Jenderson, C.P. Kubiak, W. Mahoney, R.G. Osifchin, R. Reifenverger, Science 272 (1996) 1323.
[44] T. Sagara, N. Kato, A. Toyota, N. Nakashima, Langmuir 18 (2002) 6995.
[45] T. Linnert, P. Mulvaney, A. Henglein, J. Phys. Chem. 97 (1993) 679.
[46] R.H. Doremus, J. Appl. Phys. 37 (1966) 2775.
[47] N. Cioffi, L. Torsi, L. Sabbatini, P.G. Zambonin, T. Beleve-Zacheo, J. Electroanal. Chem. 488 (2000) 42.